Investigation of protonation induced metal-to-metal electron transfer in a cyano-bridged MnIII –FeIII dinuclear complex

Prashurya Pritam Mudoi, Niku Ahmed, Anup Choudhury, Yanling Li, Rodrigue Lescouëzec, Benjamin Kintzel, Oluseun Akintola, Winfried Plass, Marimuthu Rajendiran, Nayanmoni Gogoi

Investigation of protonation induced metal-to- metal electron transfer in a cyano-bridged Mn^{III}–Fe^{III} dinuclear complex

Prashurya Pritam Mudoi,[a,b] Niku Ahmed,[a] Anup Choudhury, [a] Yanling Li, [c] Rodrigue Lescouëzec,[c] Benjamin Kintzel,[d] Oluseun Akintola,[d] Winfried Plass,[d] Marimuthu Rajendiran [a] and Nayanmoni Gogoi [a]

Reaction of [Mn(salophen)Cl] {salophen^{2-} = *o*-phenylenediamine bis(salicylidenaminato)} with a tricyano Fe(III) precursor complex, $[Fe(bbp)(CN)_3]^{2-}$ {H_2bbp = bis(2-benzimidazolyl)pyridine}, affords a dinuclear cyano-bridged heterometallic Mn^{III}(μ-NC)Fe^{III} fragment in the complex salt $[Mn(salophen)(H_2O)_2][Mn(salophen)(H_2O)(\mu\text{-}NC)Fe(bbp)(CN)_2]\cdot 4H_2O$ (1). The title compound shows field-induced slow relaxation of magnetization below 2.8 K. Possibility of a protonation induced metal-to-metal electron transfer (MMET) process in the parent complex is probed by UV-visible, electrochemical, and electron spin resonance studies.

1. Introduction

Observation of single molecule magnet (SMM) characteristics in a dodecanuclear mixed valent Mn(III)–Mn(IV) molecular cluster in 1993 triggered an outburst of activities to design molecular magnetic materials for advanced spintronic applications.[1,2] Over the last three decades, a plethora of molecular magnetic materials with intriguing characteristics have been developed. Experimental as well as theoretical exploration of these molecular magnetic materials have revealed the key principles involved in designing materials with advanced characteristics.[3] Recent observations of single molecule magnetic behavior in mononuclear lanthanide complexes at above cryogenic temperatures remain a major milestone achieved in this domain.[4,5] Apart from that, the discovery of photo-induced MMET coupled spin transition in an Fe–Co Prussian Blue Analogue (PBA) by Hashimoto and coworkers in 1996 is recognized as another key landmark in molecular magnetism.[6]

Development of molecular counterparts of Co–Fe PBA by employing capping ligands and their structure–property correlation have considerably augmented our understanding on the origin of external stimuli triggered MMET behavior.[7,8] In particular, the significance of redox potentials of the constituent Fe/Co fragments in the associated interconversion of diamagnetic Fe^{II}_{LS}-(μ-CN)-Co^{III}_{LS} state into a paramagnetic Fe^{III}_{LS}-(μ-CN)-Co^{II}_{HS} state is well recognized.[8,9] This has eventually allowed rational design of switchable magnetic materials where MMET coupled spin transition can be triggered by a varied range of external stimulants, *e.g.*, temperature, light, pressure, sol- vation-desolvation, protonation, *etc.*[7,10–15]

Despite the tremendous growth in the development of single molecule magnets, stimuli responsive switchable magnetic materials during the last three decades, examples of magnetic materials displaying both the characteristics are scarce. The majority of switchable charge-transfer materials reported so far are based on Co–Fe PBA or their molecular analogues and typically thermally induced MMET coupled spin transition to the diamagnetic Fe^{II}_{LS}-(μ-CN)-Co^{III}_{LS} phase in these systems occur well above the temperature at which SMM behavior is observed.[8–11,14] Thus, concurrent observation of MMET coupled spin transition and SMM behavior in Co–Fe (molecular) PBAs is difficult to achieve. Nevertheless, Co–Fe PBAs containing unequal proportions of Co/Fe fragments showing both MMET coupled spin transition behavior along with SMM characteristics have been recently reported.[16] This is to be associated with the occurrence of anisotropic Co(II) ions at low temperature that are not involved in MMET coupled spin transition. Moreover, in a few cases a photo-induced paramagnetic Fe^{III}_{LS}-(μ-CN)-Co^{II}_{HS} state is accessible at low temperature and SMM behavior of such light induced

[a]*Department of Chemical Sciences, Tezpur University, Napaam 784028, Sonitpur, Assam, India. E-mail: ngogoi@tezu.ernet.in*
[b]*Department of Chemistry, Dibrugarh University, Dibrugarh 786004, Assam, India*
[c]*Institut Parisien de Chimie Moléculaire, CNRS UMR 8232, Sorbonne Université, 4 place Jussieu, 75252 Paris cedex 05, France*
[d]*Institut für Anorganische und Analytische Chemie, Friedrich-Schiller-Universität, Humboldtstraße 8, 07743 Jena, Germany*
[e]*Organometallics and Materials Chemistry Lab, Department of Chemistry, Indian Institute of Technology Bombay, Mumbai 400076, India*

excited spin state are also observed in a Co–Fe molecular PBA recently.[17] Thus, bridged bimetallic systems where both the spin states accessible by MMET coupled spin transition are paramagnetic and eventually magnetically anisotropic in nature are potential candidates to design SMMs which show external stimuli responsive MMET coupled spin transition characteristics.[16] In this regard, the abundance of Mn(III) based SMMs, along with the rich redox chemistry inherent to manganese, establish the pertinence of incorporating Mn(III) fragments in such heterobimetallic complex systems.[18–21] In view of this, plethora of heterobimetallic molecular PBAs incorporating cyano-bridged Mn(III) fragments are developed and several such heterobimetallic complex systems display SMM characteristics.[8,20–23] However, MMET coupled spin transition behavior is limited to only one $\{Fe_4Mn_4\}$ molecular cube, $Cs \subset \{[Mn(pzTp)]_4[Fe(Tp)(CN)_3]_4\}\cdot 16CH_3CN$ (Tp = hydrotris(pyrazol-1-yl)borate and pzTp = tetrakis(pyrazol-1-yl) borate), which shows thermal spin state switching between the $\{Fe^{II}$-(μ-CN)-$Mn^{III}\}$ and $\{Fe^{III}$-(μ-CN)-$Mn^{II}\}$ pair.[24]

The ability to induce MMET coupled spin transition by employing external stimuli other than temperature is another viable route for development of MMET coupled spin transition active SMMs. It is pertinent to note here that the protonation of N-donor blocking ligands present on the constituent metallic fragments in several molecular PBAs have been successfully implemented as an efficient tool to facilitate MMET coupled spin transition.[12,25,26] Herein, we have employed a unique tricyano Fe(III) linker, $[Fe(bbp)(CN)_3]^{2-}$, capable of undergoing considerable redox variation upon protonation which can eventually trigger MMET coupled spin transition in coupled systems.[27] Reaction of the tricyano linker with $[Mn^{III}(salophen)]^+$ (salophen = *o*-phenylenediaminebis(salicylidenaminato))[28] resulted a cyano-bridged heterometallic fragment in the complex salt $[Mn(salophen)(H_2O)_2][Mn(salophen)(H_2O)(\mu\text{-}NC)Fe(bbp)(CN)_2]\cdot 4H_2O$ (1). Spectroscopic, structural, and electrochemical studies of this cyano-bridged Mn(III)–Fe(III) fragment along with its SMM characteristics and studies on protonation induced MMET coupled spin transition behavior are elaborated in this manuscript.

2. Results and discussion

The equimolar reaction of [Mn(salophen)Cl] and $(TBA)_2[Fe(bbp)(CN)_3]$ (TBA = Tetrabutylammonium) in methanol at room temperature afforded green plate shaped crystals of $[Mn(salophen)(H_2O)_2][Mn(salophen)(H_2O)(\mu\text{-}NC)Fe(bbp)(CN)_2]\cdot 4H_2O$ (1) (Scheme 1). Analytical, structural, spectroscopic, electrochemical, and magnetic characterizations of 1 agree well with the proposed formulation and reveal that it is a cyano-bridged Mn^{III}–Fe^{III} dinuclear complex containing an additional $[Mn(salophen)(H_2O)_2]^+$ unit as counter cation.

Molecular structure of compound 1

Compound 1 crystallizes in the monoclinic $P2_1$ space group (Table S1). The molecular structure of 1 depicted in Fig. 1 shows the presence of $\{Mn(salophen)(H_2O)\}^+$ and $\{Fe(bbp)(CN)_3\}^{2-}$ units bridged by cyano ligands resulting in a dinuc-

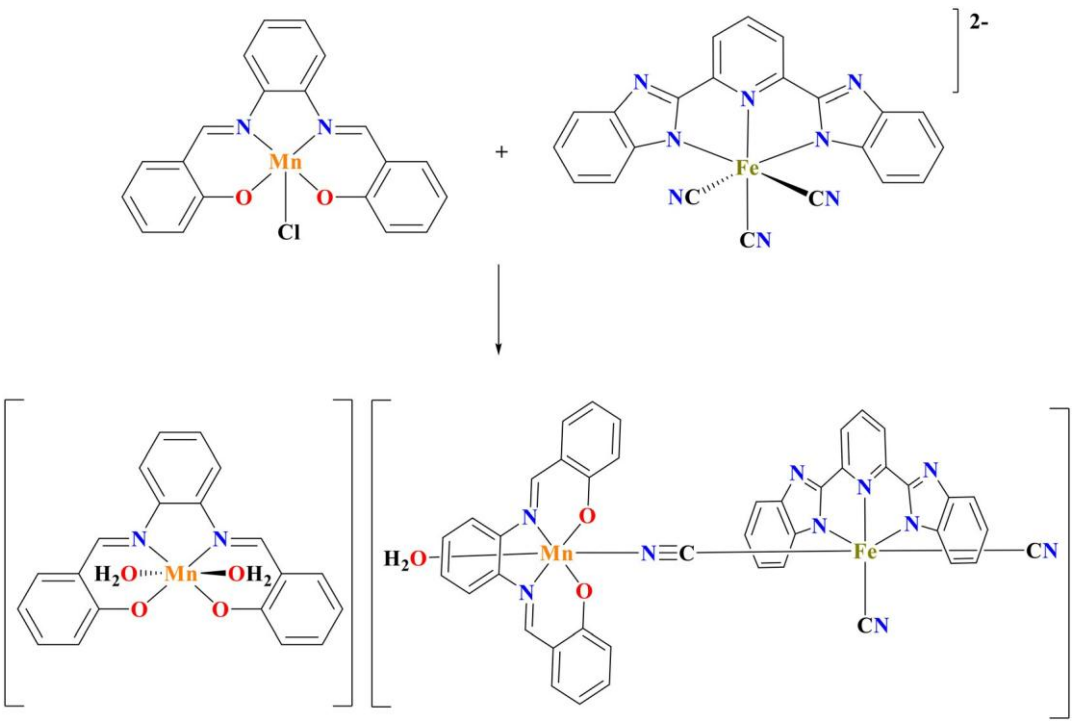

Scheme 1 A schematic representation of the synthetic route to 1.

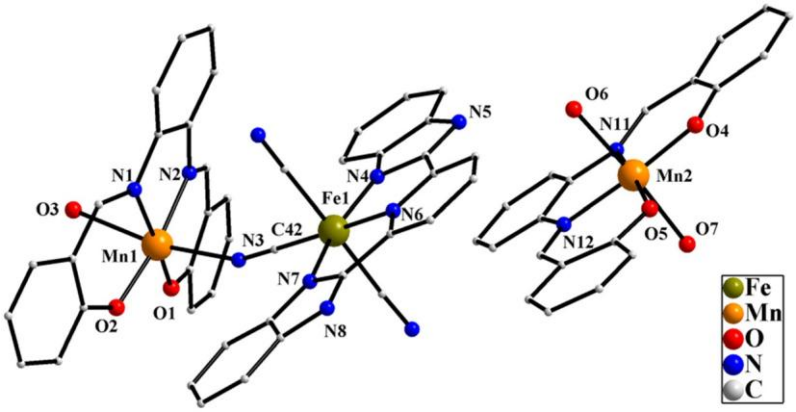

Fig. 1 Molecular structure of compound 1. All hydrogen atoms have been omitted for the sake of clarity.

lear heterometallic Mn^{III}–Fe^{III} complex fragment. A $[Mn(salophen)(H_2O)_2]^+$ complex cation is also present in the lattice for maintaining electroneutrality. The thermal ellipsoid plot (50% probability) of the asymmetric unit of 1 is depicted in Fig. S4. Selected bond distances and bond angles of 1 are documented in Table S2.

Both of the Mn^{III} centers (Mn1 and Mn2) present in 1 adopt a Jahn–Taller elongated octahedral coordination environment and four of the coordination sites are occupied by N/O donor atoms of the tetradentate Schiff-base ligand salophen. In addition to these, one of the Mn^{III} centers (Mn1) is linked to $\{Fe^{III}(bbp)(CN)_3\}^{2-}$ moiety *via* a cyano group with the remaining coordination site of this Mn^{III} center being occupied by an aqua ligand. Thus, the Mn1 center has a N_3O_3 coordination environment. However, both axial coordination sites of the non-bridged Mn^{III} center (Mn2) are occupied by aqua ligands rendering this Mn^{III} center to have an N_2O_4 coordination environment. As documented in Table S2, the Mn–O_{aquo} and Mn–$N_{cyanide}$ bond lengths are considerably longer than the Mn–$N_{salophen}$ and Mn–$O_{salophen}$ distances resulting in an axially elongated octahedral geometry around the Mn1 and Mn2 centers, and this can be attributed to Jahn–Teller distortion in high spin Mn^{III}. The Fe^{III} center present in the $[Fe^{III}(bbp)(CN)_3]^{2-}$ moiety in 1 adopts a distorted octahedral coordination geometry with C_3N_3 coordination environment like in the cyanometallate precursor complex. Only one out of the three cyano groups available in $[Fe^{III}(bbp)(CN)_3]^{2-}$ is involved in bridging coordination of a Mn^{III} center, while the other two cyano groups remain terminal. The average Fe–N_{bbp} distances are measured to range from 1.937 to 1.970 Å (Table S2) and the observed distances exhibit values close to the related low spin Fe^{III} species.[12,25] The Mn–N–C and Fe–C–N bond angles are 155.20 and 179.13° (Table S2), respectively, and fall in the expected range and consequently separate the two metallic centers by about 5.134 Å.

In 1, intramolecular H-bonding is operative between the axial aquo group (O6) of the free $[Mn(salophen)(H_2O)_2]^+$ and the imidazole N-atom of $[Mn(salophen)(H_2O)(\mu\text{-}NC)Fe(bbp)(CN)_2]$ fragment (O6–H6B···N5) (Fig. S6). Further, one of the H atoms (H3B) of the axial aqua group coordinated to the bridged $[Mn(salophen)(H_2O)]^+$ moiety interacts through intermolecular hydrogen bonding (O3–H3B···N10) with N atoms of a free cyano ligand in the $[Fe^{III}(bbp)(CN)_3]^{2-}$ fragment of a nearby Mn^{III}–Fe^{III} dinuclear complex (Fig. 2). This leads to the formation of a H-bonded one-dimensional network in a *zig-zag* fashion with an intermolecular separation of 10.537 and 9.097 Å between the respective Fe^{III} and Mn^{III} centers (Table S4).

UV-visible absorption spectroscopic studies of 1

The electronic spectra for the precursor Mn^{III} salophen complex [Mn(salophen)Cl], cyanometallate $(TBA)_2[Fe(bbp)(CN)_3]$, and 1 were recorded in DMSO medium (Fig. S7). Under an ideal symmetric octahedral ligand field, the electronic transition $^5T_{2g} \leftarrow {}^5E_g$ state is expected for a high-spin d^4 Mn^{III} system.[29] However, the electronic spectra of most pseudo-octahedral Mn^{III} compounds are found to be complicated owing to the static and dynamic Jahn–Teller effects that perturb the octahedral symmetry. UV-visible spectra of the precursor [Mn(salophen)Cl] and 1 between 300–500 nm are identical in shape and consist of two regions of absorption. The broad band around 400–500 nm can be assigned to ligand-to-metal charge transfer (LMCT) band between salophen and Mn^{III} centers.[21] The other intense band observed between 250–380 nm can be attributed to the π to π^* transition of the aromatic salophen ligand.[29] The intense band centered around ~618 nm observed in the UV-visible spectra of compound 1 can be assigned to LMCT within the $\{Fe^{III}(bbp)(CN)_3\}$ unit (Fig. S7).[25] Thus, the correlation of UV-visible spectra of 1 with those of individual precursor molecules reveal that both the constituent fragments, $\{Mn^{III}(salophen)\}^+$ and $\{Fe^{III}(bbp)(CN)_3\}^{2-}$ are present in 1 without undergoing any changes in oxidation state. UV-visible diffuse reflectance spectra of 1 (Fig. S8) shows strong resemblance with the recorded spectra in DMSO solution and thereby suggests that compound 1 well preserved its structural integrity upon dissolution. The ESI-MS fragmentation pattern of 1 shows *m/z* values corresponding to both the molecular ion and other cyano-bridged entities (Fig. S9 and S10), demonstrating the

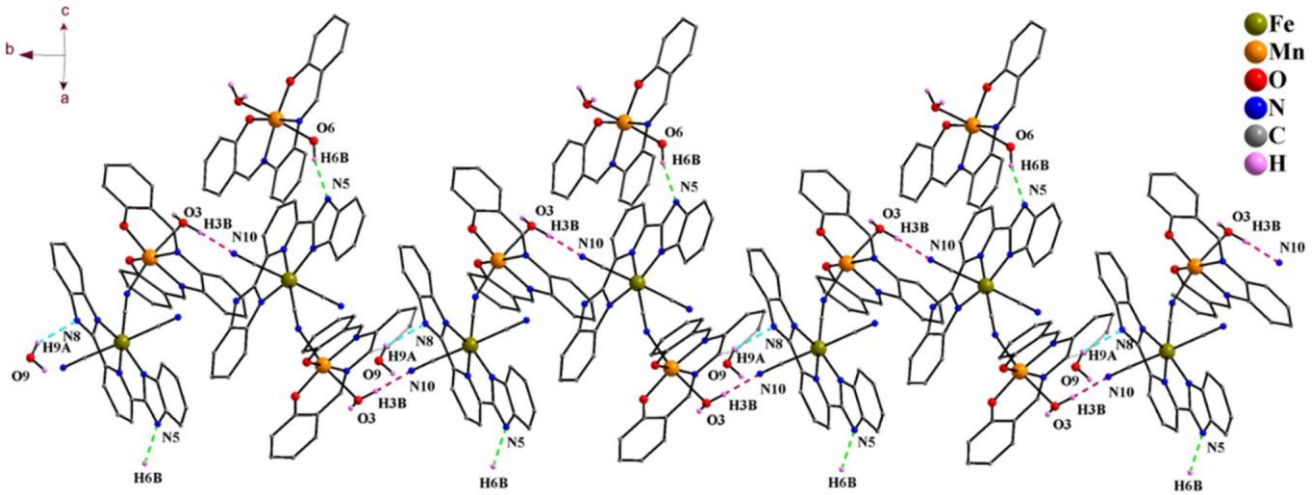

Fig. 2 Interchain O–H···N hydrogen bonding network in 1. Aromatic hydrogen atoms have been omitted for clarity. Three different types of H-bonding are shown in different colors. (N5···H6B = green; N10···H3B = pink and N8···H9A = cyan).

integrity of the cyano-bridged heteronuclear Mn(III)–Fe(III) structures in DMSO medium.

Electrochemical properties of 1

In order to probe the electronic states, electrochemical responses of both the precursor complexes and 1 were investigated by cyclic voltammetry in DMSO medium with 0.1 M *n*-Bu_4NPF_6 as supporting electrolyte and a scan rate 100 mV s^{-1} at room temperature. A reversible peak observed at $E_{1/2}$ = −0.80 V (*versus* Ag/AgCl) in the cyclic voltammogram of 1 can be assigned to the Fe^{III}/Fe^{II} redox couple (Fig. 3 and Table S5). The moderate shifting of this redox couple as compared to the precursor $(TBA)_2[Fe(bbp)(CN)_3]$ (Fig. S11) upon bridged to $[Mn(salophen)]^+$ is consistent with the fact that the electron density is being redistributed across the shared cyano ligand.[25] Furthermore, the anodic region of the cyclic voltammogram (CV) of 1 reveals one reversible process at $E_{1/2}$ = −0.12 V. It is pertinent to note that the redox behavior of (phenoxy) manganese complexes was found to be complicated due to the observation of both metal- and ligand centered electron transfer processes at accessible potential ranges. In fact, Mn^{III}-phenolato complexes often show both Mn^{III}/Mn^{II}, Mn^{IV}/Mn^{III} redox couples.[21,30–32] Nevertheless, based on redox studies on the precursor Mn^{III}-salophen complex, the redox process observed at $E_{1/2}$ = −0.12 V can be assigned to Mn^{III}/Mn^{II} redox couple (Fig. S11). Interestingly, when CV of 1 was measured up to an applied voltage of 1.50 V, a new irreversible peak is observed at $E_{1/2}$ = 0.06 V (Fig. S19). This peak can be attributed to reduction of side products generated due to overoxidation of the complex and observed in case of the tricyanometalate precursor, $(TBA)_2[Fe(bbp)(CN)_3]$ as well (Fig. S22).

ESR spectroscopic characterization of 1

CW X-band ESR spectroscopic studies of 1 were performed on both a frozen DMSO solution at 84 K and a solid powder, with

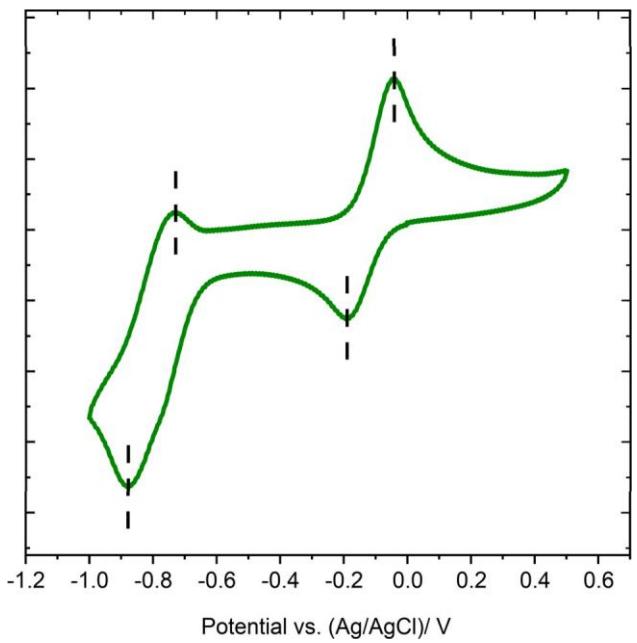

Fig. 3 Cyclic voltammogram of 1 measured in 0.1 M electrolyte at a scan rate of 100 mV s^{-1}.

the corresponding spectra depicted in Fig. 4 and Fig. S12, S13, respectively. The spectra are dominated by a signal characteristic of an Fe^{III}_{LS} species, which was simulated using an axial *g*-tensor model with parameters $g_{x,y}$ = 2.30 and g_z = 1.89 for the frozen solution, and $g_{x,y}$ = 2.29 and g_z = 1.90 for the powder spectrum. The linewidth was modeled exclusively with isotropic Lorentzian line broadening (frozen solution: 4.5 mT; powder: 6 mT). These results are consistent with the presence of an Fe^{III}_{LS} center in complex 1 and allow for precise spectral parameterization.

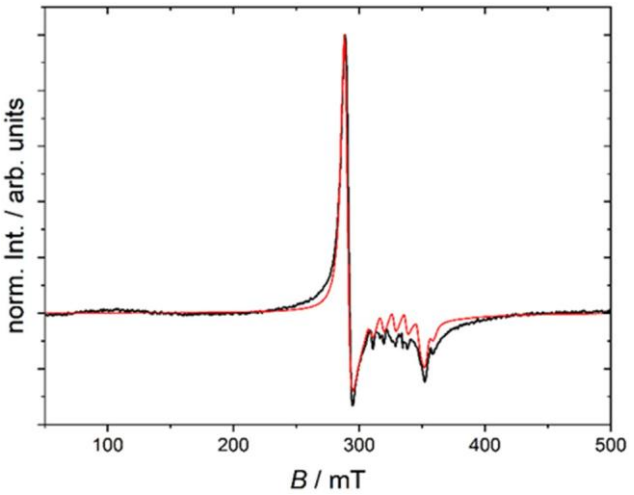

Fig. 4 CW-X-band ESR spectrum of 1 dissolved in DMSO at 84 K recorded with a microwave frequency of 9.298 GHz. The black line represents the experimental spectrum, the red line is a simulation using two components with the parameters mentioned in the text and in Table S6.

In contrast, the signals from the Mn^{III} centers, both in the complex anion and the counter cation, are not distinctly visible in the spectra. This observation is consistent with literature reports on Mn^{III} systems, where strong line broadening and signal overlap typically obscure direct detection. The broad features observed around B = 100 mT, along with some arbitrary intensity variations extending across the spectral range up to 600 mT, can be attributed to contributions from the Mn^{III} ions. These broad signals are characteristic of Mn^{III}-based salen-type complexes and are consistent with previous observations of comparable systems.[33] Therefore, a spectral parametrization of the Mn^{III} contributions was not feasible.

In addition, a minor signal corresponding to a Mn^{II}_{HS} species was detected. This signal exhibits the characteristic six-line hyperfine splitting caused by coupling with the ^{55}Mn nucleus, further supported by observations in the protonation studies (*vide infra*). The signal was simulated with an isotropic g-value of 1.99 for the frozen DMSO solution (powder spectrum: 2.077) and a hyperfine coupling constant of A = 270 MHz. The Mn^{II} impurity is present in a molar fraction of 0.3% relative to the Fe^{III}_{LS} component and is detectable due to its larger, purely isotropic spin (S = 5/2), its lower Lorentzian line broadening (3.5 mT in frozen solution), and the highly discriminating nature of the detection mode in CW-ESR experiments.

All parameters used for the simulation of the Fe^{III}_{LS} and Mn^{II} signals are summarized in Table S6. A separate depiction of the contributing subspectra for the frozen DMSO solution case is given in Fig. S13. From the interpretation of the data, it can be concluded that the coordination environment around the Fe^{III}_{LS} center does not undergo significant changes upon dissolution in DMSO, as evidenced by the virtually unchanged g-tensor parameters. In contrast, the nature of the Mn^{II}_{HS} impurity remains unclear in both the solution and solid-state spectra, leaving its origin enigmatic. Furthermore, the relatively large isotropic Lorentzian line broadening observed for Fe^{III}_{LS} in frozen DMSO solution (4.5 mT) suggests that the bridging coordination to the spin-bearing Mn^{III}_{HS} center is preserved. This implies an interaction between the two electronic spins, leading to spin-spin relaxation and contributing to the observed line broadenings.

Variable temperature magnetic properties of 1

DC magnetic properties of 1. The experimental and theoretical variation of $\chi_M T$ *versus* T of 1 is depicted in Fig. 5a. The room temperature $\chi_M T$ value of 1, 6.40 $cm^3\ K\ mol^{-1}$, is close to the expected $\chi_M T$ product of 6.50 $cm^3\ K\ mol^{-1}$ for two magnetically isolated Mn^{III}_{HS} centers (S = 2, g = 2) and one Fe^{III}_{LS} center (S = 1/2, g = 2.3). Upon cooling the $\chi_M T$ value of 1 is almost constant between 300–40 K and shows a gradual decrease between 40–10 K, indicating an antiferromagnetic coupling between the cyano-bridged high spin Mn^{III} and low spin Fe^{III} ions. Below 10 K, the $\chi_M T$ value decreases abruptly down to a minimum value of 3.78 $cm^3\ mol^{-1}$ K at 2 K. This sharp downturn at low temperature is associated with the zero-field splitting and/or antiferromagnetic intermolecular interactions, comparable to those observed in case of earlier reported cyano-bridged {Mn^{III}–Fe^{III}} bimetallic complexes (Table S8).[34–40] The experimental $\chi_M T$ values of 1 between 300 and 2 K were analyzed using the following spin Hamiltonian and PHI software:[41]

$$H = -J(S_{Fe} \cdot S_{Mn}) + \beta H[g_{Fe} \cdot S_{Fe} + 2g_{Mn} \cdot S_{Mn}] + 2D_{Mn} \cdot S_{zMn}^{\ 2} \quad (1)$$

The first term in eqn (1) deals with the isotropic magnetic interactions between Mn^{III} and Fe^{III} centers, J being the magnetic coupling constant and S_M [M = Fe^{III} and Mn^{III}] stands for the spin operators of Fe^{III} and Mn^{III}, respectively. The second term represents the Zeeman interactions of the cyano-bridged bimetallic entity and of the counter-ion, with g_{Fe} and g_{Mn} as the g-factors of Fe^{III} and Mn^{III}, β as Bohr magneton and H, as magnetic field. The third term considers the average axial zero-field splitting (zfs) parameter of the Mn^{III} ions in both the bimetallic complex (Mn1) and the counter-ion (Mn2). To constrain the fitting parameters, the two Mn^{III} ions were assumed to have the same axial zfs parameter (D_{Mn}), and a g_{Mn} = 2.0 from the literature was used.[42] The anisotropic g-value for Fe^{III} from the ESR measurements for the powder sample ($g_{x,y}$ = 2.29 and g_z = 1.90) has been fixed in the input file, along with a parameter representing the antiferromagnetic intermolecular interactions (zJ = −0.025 cm^{-1}), to adjust the low-temperature $\chi_M T$ data. The best-fit Hamiltonian parameters are: J = −4.27 cm^{-1}, and D_{Mn} = −2.1 cm^{-1} with a TIP (temperature independent paramagnetic) component of -1.07×10^{-3} $cm^3\ mol^{-1}$ and a residual value (Res) of 0.1504. The definition of the fitting residual is: Res = $[\Sigma(M_{exp} - M_{cal})^2]\ [\Sigma(\chi_{exp} - \chi_{cal})^2]$. The D_{Mn} value derived from the fitting of $\chi_M T$ *versus* T data lies within the D_{Mn} value range of −4 to −1 cm^{-1} reported in the literature.[42]

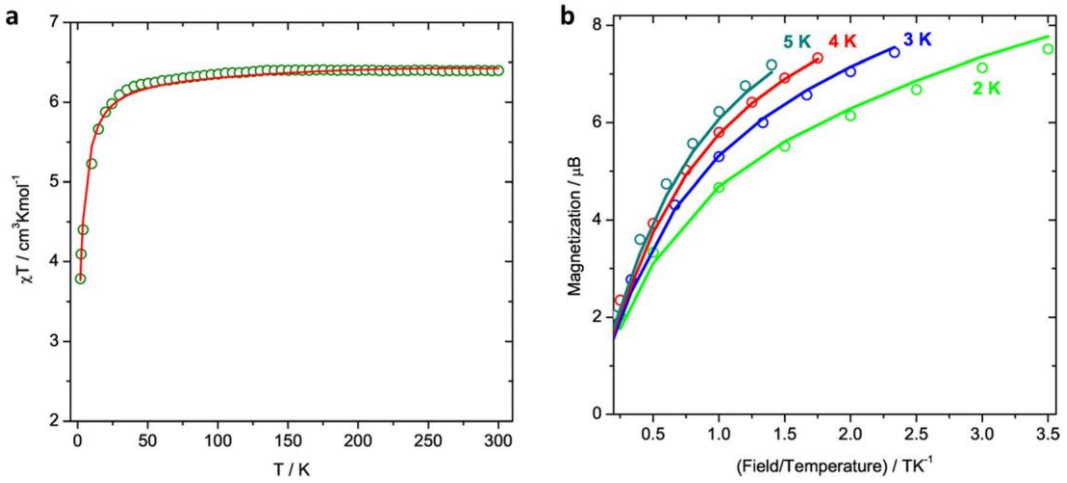

Fig. 5 Experimental (circles) and theoretical (red line) $\chi_M T$ *versus* T of 1 between 2–300 K (a). Experimental (circles) and theoretical (solid lines) M *versus* H/T of 1 between 2–5 K and 0.5–7 T (b).

The reduced magnetization (M) measurements of 1 have been carried out between 0.5–7 T and 2–5 K. The M *versus* H/T curves under different magnetic field are not superimposable (see the Fig. 5b). This could originate from two facts: (i) the anisotropy of the Mn1 and Mn2 centers and (ii) the weak magnetic coupling constant J.[43] M attains a value of 7.5 $\mu\beta$ at 7 T which is smaller than the theoretical value of 9 $\mu\beta$ obtained from S_{Mn} and S_{Fe} assuming g = 2.0, due to the significant magnetic anisotropy of 1.

As the simultaneous fitting of $\chi_M T$ *versus* T and M *versus* H/T data did not give satisfactory results, we have calculated M *versus* H/T separately using eqn (1), employing the values J = −4.27 cm^{-1}, the anisotropic g_{Fe} ($g_{x,y}$ = 2.29 and g_z = 1.90), and g_{Mn} = 2.0. The parameters to be optimized are the average axial and rhombic zfs parameters of the Mn1 and Mn2 centers (D_{Mn} and E_{Mn}). A satisfying fit is achieved, provided that the data at 6 and 7 K are excluded, leading to D_{Mn} = −4.94 cm^{-1} and E_{Mn} = 0.31 cm^{-1}. The D_{Mn} value is much greater than that derived from the fitting of the temperature-dependent magnetization data (−2.1 cm^{-1}). This discrepancy can be explained by the exchange interaction between Fe(III) and Mn (III) bridged by cyanide, which becomes significant at temperatures below 6 K, resulting in a more anisotropic low-temperature electronic structure compared to that at higher temperature (T > 6 K).

AC magnetic properties of 1. To examine the slow relaxation dynamics of 1, alternating current (ac) susceptibility measurements were performed at zero dc field. The measurements revealed the absence of frequency-dependence in the in-phase (χ'_M) and out-of-phase (χ''_M) signals down to 2 K (Fig. S14). However, upon applying a static dc field of 0.16 mT, both χ' and χ'' show clear frequency-dependence below 3.5 K, indicating the field-induced SMM behavior of 1. Fig. 6 shows the variation of χ''_M *versus* χ'_M (CCP = Cole–Cole Plots) and *versus* frequency in logarithmic scale at different temperatures from 2 to 3.3 K.

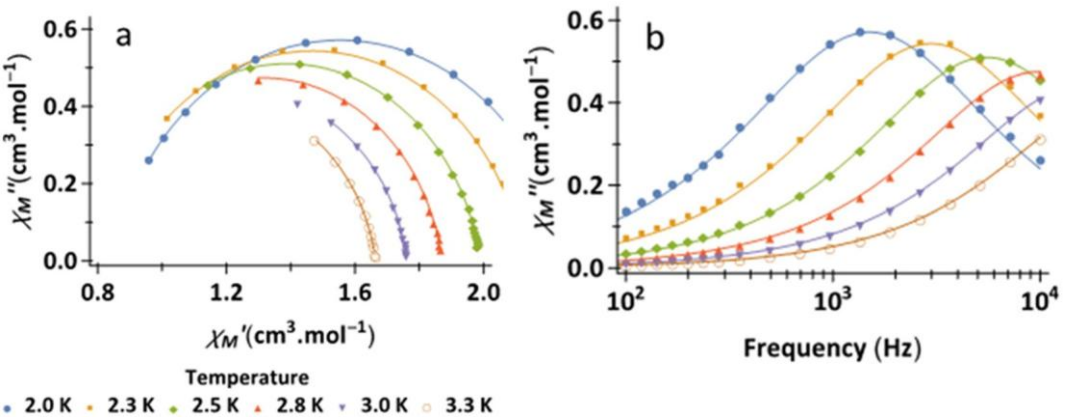

Fig. 6 CCP at different temperatures (a) and χ'_M' *versus* frequency in logarithmic scale (b) for 1 between 2 and 3.3 K at an applied static dc-field of 0.16 mT.

The variation of χ'_M *versus* T is shown in the supplementary section (Fig. S15). As the structural similar, antiferromagnetically coupled Mn^{III}–Fe^{III} dinuclear complex is not a SMM,[44] the field-induced SMM behavior is probably due to Mn^{III} in the counter-ion. The fitting of the CCP and χ''_M *versus* frequency data into a generalized Debye model by using a home-made Mathematica® program gives the parameters characterizing the slow relaxation of magnetization of 1, which are summarized in the Table 1. χ_s and χ_t are the minimum and maximum values of χ'_M , respectively, corresponding to $\chi''_M = 0$. α represents the distribution of the relaxation process, its value is between 0 and 1. α close to 0 indicates a one-process relaxation and α close to 1, a multi-process relaxation. τ is the relaxation time. The plot of $\ln(\tau)$ against $1/T$ gives a straight line, stipulating that the slow relaxation of 1 obeys an Arrhenius law:

$$\ln(\tau) = \ln(\tau_0) + U_{eff}/(k_B T) \quad (2)$$

where U_{eff} is the energy barrier of slow relaxation and τ_0, the intrinsic relaxation time of 1. The linear regression of $\ln(\tau)$ against $1/T$ (see Fig. S15) gives: $\ln(\tau) = -16.536 + 15.093/(k_B T)$. This allows us to deduce the values of τ_0 and of U_{eff} $\tau_0 = 6.58 \times 10^{-8}$ s and $U_{eff} = 15.09$ K (10.49 cm^{-1}). The energy barrier of 1 is comparable to that of the 1D chain $[Mn_2(saltmen)_2Fe(LN_5)(CN)_2]^{2+}$ which is also a field-induced SMM with U_{eff} = 13.9 K.[45] In this compound, the oxo-bridged Mn^{III} dinuclear units are ferromagnetically coupled and they are linked into a 1D chain by the diamagnetic moiety $[Fe(LN_5)(CN)_2]$.

Investigation of protonation-induced electron transfer in 1 by UV-visible spectroscopy

Protonation assisted MMET coupled spin transition behaviors have been witnessed recently in few cyano-bridged heterometallic dinuclear[25] and square[12,26] complex systems that incorporate a $[Fe^{III}(bbp)(CN)_3]^{2-}$ fragment as linker. The uncoordinated benzimidazole N-atoms of the $[Fe^{III}(bbp)(CN)_3]^{2-}$ fragment can be protonated and this in turn substantially modifies the redox potential of the Fe^{III}/Fe^{II} couples. The presence of the $[Fe^{III}(bbp)(CN)_3]^{2-}$ fragment in the dinuclear cyano-bridged $\{Mn^{III}$-μ-NC-$Fe^{III}\}$ complex unit of 1 motivated us to explore the possibility of protonation induced electron transfer behavior in compound 1. To investigate the feasibility of the electron transfer interaction, the evolution of the UV-visible spectra of a 3.12×10^{-4} M solution of 1 (Fig. 7) and precursor complex [Mn(salophen)Cl] in DMSO upon addition of successive aliquots of trifluoroacetic acid (TFA) was recorded. No significant spectral changes were observed in the UV-visible spectra of the precursor compound [Mn(salophen)Cl] upon addition of TFA (Fig. S17), confirming its stability under acidic environment. However, a naked eye discernible alternation of color from green to orange with a concomitant depletion of the absorption band at 618 nm, was observed in case of 1 with increasing TFA concentration (Fig. 7).[12,25] Simultaneously, emergence of a new absorption band with a maximum at 533 nm is observed. This broad absorption feature is assigned as metal-to-ligand charge transfer (MLCT) transition from Fe^{II} to the bbp in protonated 1.[12,25] The observed spectral modification upon controlled acidification suggests protonation of the uncoordinated benzimidazole N-atoms and perfectly resembles with spectral changes observed in case of earlier reported cyano-bridged complex systems containing an $[Fe^{III}(bbp)(CN)_3]^{2-}$ fragment.[25,26] Moreover, the intensity of the band in the range 400–500 nm assigned to LMCT between salophen and Mn center increases substantially upon acidification. This progressive enhancement of absorbance can be attributed to decrease in electron density on the Mn center on TFA addition and concomitant augmentation of transition dipole moment. Thus, protonation induced disappearance of the bbp to Fe^{III} LMCT band at 618 nm, appearance of the Fe^{II} to bbp MLCT band at 533 nm and progressive increase in absorbance of salophen to Mn LMCT band suggest interplay of metal-to-metal electron transfer within the cyano-bridged Mn^{III} and Fe^{III} centers (Fig. 7).

Furthermore, the spectral changes observed upon addition of successive aliquots of TFA to a DMSO solution of 1 show an isosbestic point around ~560 nm. It thereby hints that only two species are involved in the protonation induced electron transfer process. However, the evolution of the two characteristic bands at 618 and 533 nm representing LMCT and MLCT, respectively, are non-ratiometric. Apart from that, the curves representing normalized absorbances at these two characteristic wavelengths exhibit a crossing point below an absorbance of 0.5. The above two observations suggest the interplay of more than two species in solution subsequent to protonation of 1.

Investigation of protonation-induced electron transfer in 1 by cyclic voltammetry

Protonation induced UV-visible spectroscopic investigations suggest an interplay of electron transfer within the metal centers present in 1. To gain better insight into the protonation induced electron transfer process in solution state, the effect of protonation on the redox potentials of the constituent metal centers has been explored in DMSO medium. Upon addition of successive aliquots of TFA (up to 10 equivalent), significant changes in the electrochemical behavior of 1 are observed (Fig. 8, and S18).

After addition of six equivalents TFA to 1, the reversible redox wave at $E_{1/2} = -0.12$ V assigned to the Mn^{III}/Mn^{II} couple disappears completely. No such changes in redox behavior are observed upon addition of acid to the precursor Mn^{III}-salophen complex (Fig. S20). Therefore, the observed electrochemical changes upon addition of TFA to 1 can be attributed

Table 1 Parameters of the slow relaxation process of 1

T (K)	χ_s ($cm^3\ mol^{-1}\ K$)	χ_t ($cm^3\ mol^{-1}\ K$)	α	$\tau \times 10^{-6}$ (s)
2.031	0.846	2.262	0.136	105.65
2.263	0.806	2.127	0.124	52.72
2.509	0.784	1.991	0.106	28.41
2.755	0.758	1.872	0.102	16.53
3.009	0.729	1.762	0.101	10.09
3.254	0.688	1.665	0.103	6.31

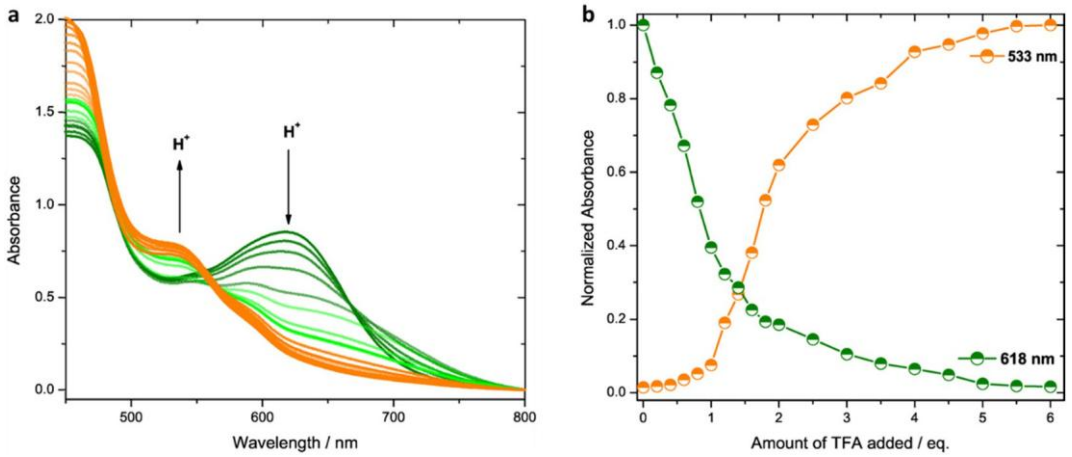

Fig. 7 Evolution of UV-visible absorption spectra of a 3.12×10^{-4} M DMSO solution of 1 upon addition of successive aliquots of TFA (a) and normalized absorbance at 533 and 618 nm against the amount of TFA added from green to orange, the acid addition occurs with an interval of (i) 0.2 equivalents up to 2 equivalents (ii) 0.5 equivalents up to 6 equivalents (b).

to changes in electronic environment of the Mn center in 1 triggered by protonation of bbp ligand in the constituent [Fe(bbp)$(CN)_3$] fragment. While the Mn^{IV}/Mn^{III} redox wave expected above 0.5 V is not observed in cyclic voltammogram of 1 after TFA addition.

Moreover, upon addition of 6 equivalents TFA to 1, the reversible redox wave corresponding to Fe^{III}/Fe^{II} at $E_{1/2} = -0.80$ V disappear and simultaneously a new irreversible redox wave appears at $E_{cathodic} = -0.66$ V because of protonation in [Fe(bbp)$(CN)_3]^{2-}$ fragment of 1. Apart from that, emergence of a new reversible redox wave at $E_{1/2} = 0.12$ V can be attributed to the metal to metal electron transfer mediated formation of Fe(II) in the cyano-bridged unit of 1 upon protonation in the probing medium.[25] These changes in redox behavior of the Fe(III)/Fe(II) couple in 1 is comparable to the changes observed for the precursor, $[Fe(bbp)(CN)_3]^{2-}$ (Fig. S21) as well as in case of cyano-bridged heterometallic Co–Fe, Mn–Fe, Ni–Fe complex systems containing this tricyano iron(III) fragment.[12,25,26,46] The positive shift of Fe^{III}/Fe^{II} redox couples upon addition of TFA is attributed to protonation on the free nitrogen atoms in bbp ligand. This shifting of the Fe^{III}/Fe^{II} redox couples towards more positive potential during protonation minimizes the redox potential differences, ΔE between Fe and Mn centers and thereby promotes metal-to-metal electron transfer (MMET) in accordance with Marcus-Hush theory.[47] However, cyclic voltammogram of 1 after TFA addition did not show any redox wave corresponding to Mn(IV)/Mn(III) couple to conclusively establish the metal-to-metal electron transfer induced transition of the parent $\{Mn^{III}(\mu\text{-NC})Fe^{III}\}$ state to a possible $\{Mn^{IV}(\mu\text{-CN})Fe^{II}\}$ state.

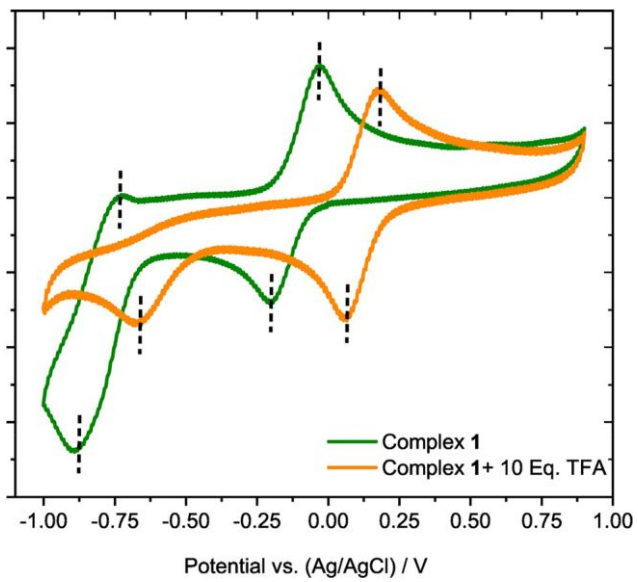

Fig. 8 Cyclic voltammogram of 1 measured in 0.01 M electrolyte at a scan rate of 100 mV s^{-1} in DMSO (Green) and 1 upon addition of 10 eq. of acid (Orange).

Investigation of protonation-induced electron transfer in 1 by ESR spectroscopy

To further probe the possibility of protonation induced electron transfer a comparable titration experiment was also monitored by means of CW X-band ESR spectroscopy. To keep the experimental conditions as close as possible to the UV/Visible and CV experiments but retain a good resolution of the spectra we chose a temperature of 230 K. First, the spectrum of pure 1 (see Fig. 9) could be well simulated using the same parameters and component ratios as for the simulation at 84 K (*vide supra*) merely adjusting the isotropic Lorentzian line broadening (12 mT for Fe^{III}_{LS} and 4 mT for Mn). Unfortunately, the presence of the Mn^{II}_{HS} corrupts an exact quantification of Fe^{III}_{LS} throughout the titration, since it overlays the signal and we do not know to what extent the impurity is changed upon acidification. Moreover, the species expected to be formed *via* electron transfer are ESR silent (Fe^{II}_{LS}) or hardly detectable at this temperature due to its spin state and relaxation behavior (Mn^{IV}).[48]

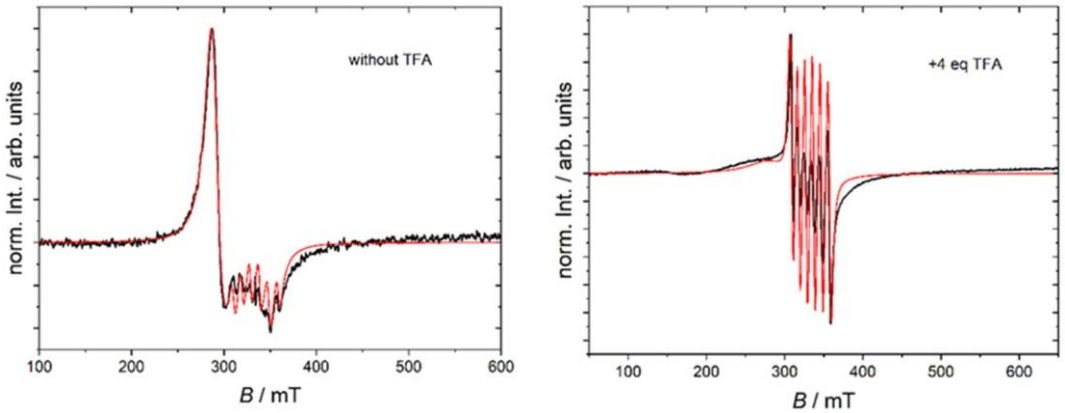

Fig. 9 CW X-band ESR spectra of 1 dissolved in DMSO recorded at 230 K in pristine state (left) and after addition of 4 equivalents of trifluoroacetic acid (right). Black lines represent the experimental spectra and red lines the corresponding simulations using the parameters given in Tables S6 and S7.

Therefore, ESR spectroscopy in this context can only provide qualitative hints about the depletion and formation of species and we have chosen the steps of the titration rather coarsely (+1 eq., +2 eq., +4 eq. TFA, depicted in Fig. 9 and Fig. S23, respectively). All spectra were simulated using the principal parameters of the spin system extracted from the spectrum of the DMSO solution at 84 K (see Fig. 4 and Table S6) and merely changing the fraction of the two components as well as the isotropic Lorentzian linewidth (lw_L).

After addition of 1 equivalent of TFA, the isotropic Lorentzian linewidth of the Fe^{III}_{LS} component increases to 20 mT and a broad feature with resonance position at ~140 mT appears, which is most likely related to the formation of Mn^{IV}. The fraction of the two spectral components necessary to simulate the spectrum changes to 99.5% Fe^{III}_{LS} and 0.5% Mn^{II}_{HS}. Hence, assuming that the amount of Mn^{II}_{HS} in the mixture is constant, this means that the molar fraction of Fe^{III}_{LS} has roughly halved. Looking at the corresponding spectra with 2 and 4 eq. TFA added, the linewidth of the Fe^{III}_{LS} component is no longer a well-determined parameter, thus, also the correlated molar fraction of 95 to 5% used for the simulation of both spectra is not a precise characteristic of the system. However, the spectra reveal to the bare eye that for 2 eq. the subspectrum of the Fe^{III}_{LS} component decreases tremendously and for 4 eq. it is hardly visible at all. Instead, the spectrum is dominated by the nicely resolved six-line hyperfine pattern of the Mn^{II}_{HS} impurity, which confirms the initial suspicion about its identity (*vide supra*). Interestingly, also the feature we ascribed to the formation of Mn^{IV} almost vanishes, which might be due to slight changes in coordination geometry making the spin system even less detectable in X-band ESR. All parameters varied with respect to the pristine spectrum at 84 K to simulate the titration spectra are listed in Table S7. In summary, the observed trends clearly confirm the mechanistic suggestions for the electron transfer in 1 raised on the basis of UV/Vis and CV experiments, especially the complete disappearance of Fe^{III}_{LS}.

3. Experimental section

Chemicals were purchased from Merck India, TCI chemicals and Sigma Aldrich India and used without further purification. Solvents were procured from Merck India and Rankem India and were distilled using common purification techniques. Schiff base ligand, H_2salophen and the precursor complex [Mn(salophen)Cl], tridentate ligand, bis(2-benzimidazolyl) pyridine, (H_2bbp) and tricyanometallate precursor, $(TBA)_2[Fe(bbp)(CN)_3]$ were prepared by following literature procedure.[27,28] Elemental analysis was performed on a Perkin Elmer Model PR 2400 Series II Elemental Analyzer. Fourier transform infrared spectra were recorded on a Perkin Elmer MIR-FIR FT-IR spectrophotometer as KBr diluted discs in the ranges from 400 to 4000 cm^{-1}. The UV-visible spectra were recorded in a Shimadzu UV 2550 spectrophotometer. For the UV-visible titration studies, 0.01 M stock solution of 1 was prepared without pre-treatment of the DMSO. The titration with trifluoroacetic acid (TFA) was carried out under room temperature conditions for 3.12×10^{-4} M solution, with acid addition in increasing interval of (i) 0.2 equivalent up to 2 equivalent (ii) 0.5 equivalent up to 6 equivalent. Thermal gravimetric analyses were performed with the help of Thermal Analyzer (Model TGA-50 and DSC-60, Shimadzu) under a nitrogen atmosphere at a rate 5 °C min^{-1} up to 500 °C. Magnetic measurements performed on microcrystalline samples with an applied field of 0.16 mT over 2–300 K temperature range using a Quantum Design SQUID magnetometer and a PPMS-9 susceptometer. Field dependent magnetization studies were performed between 0 to 7 T at 2 K. Electrochemical measurements were performed using a Metrohm Autolab PGSTATE204 potentiostate. A three-electrode set-up consisting of glassy carbon as the working electrode, a Pt wire as the counter electrode and Ag/AgCl (saturated KCl) as the reference electrode were used for measurements. In the measurement, the titrations of TFA were achieved by the addition of successive aliquots of TFA of 0.01 M stock solution to 0.01 M DMSO solution of 1. Solid

state UV-visible spectra were recorded on a Shimadzu UV-2600 spectrophotometer. Mass spectrometric analyses were performed using Agilent 6530 Accurate-Mass Q-TOFLC/MS system.

Single crystals of the compounds suitable for diffraction measurements were used directly from the reaction mixtures. The diffraction data for complex 1 was collected on a Rigaku Saturn 724 + CCD Diffractometer using MoKα radiation (λ = 0.71073 Å) using φ and ω scans of narrow (0.5°) frames at 150 K. Anisotropic refinement was executed on all non-hydrogen atoms. The aliphatic and aromatic hydrogen atoms were placed on calculated positions but allowed to ride on their parent atoms during subsequent cycles of refinements. Crystallographic data for the structure in this paper have been deposited with the CCDC 2423285 (1).

All ESR measurements were carried out on a Bruker Elexsys E580 spectrometer with an SHQE resonator using a modulation amplitude of 0.4 mT and an attenuation of 25 dB. Liquid nitrogen temperatures were achieved using a quartz cooling finger insert. The crystalline powder was ground prior to the measurement to minimize anisotropy effects. Simulations were carried out using the MatLab based EasySpin program package (version 6.0.4).[49] For the solution and titra- tion studies a 0.01 M stock solution of 1 was prepared in freshly distilled DMSO. The stepwise titration of Trifluoroacetic acid was achieved by addition of equivalent amounts of a 0.1 M stock solution in DMSO to an aliquot amount of the stock solution of 1, followed by a hang time of 5 min before transferring parts of the solution into the ESR tube and quickly freezing it in the spectrometer.

Synthesis of $[Mn(salophen)(H_2O)_2][Mn(salophen)(H_2O)(\mu\text{-}NC)Fe(bbp)(CN)_2]\cdot 4\,H_2O$ (1)

To a methanolic solution (10 mL) of [Mn(salophen)Cl] (0.0069 g, 0.020 mmol), a methanolic solution (10 mL) of $(TBA)_2[Fe(bbp)(CN)_3]$ (0.0196 g, 0.020 mmol) was added under continuous stirring at room temperature. The resulting green solution is stirred at room temperature for another one hour and then diethyl ether is allowed to slowly diffuse into it. Dark green plate shaped crystals of compound 1 were observed in the middle of the test tube after one week. The crystals were separated, washed with methanol followed by diethyl ether and collected. Yield: 0.012 g {64% based on [Mn(salophen)Cl]}. Elemental Analysis: found (calculated for $C_{62}H_{51}FeMn_2N_{12}O_{11}$): C, 56.81% (57.02%); H, 3.54% (3.94%); N, 11.96% (12.87%). FT-IR (KBr, ν cm^{-1}): 3422(s), 2925(s), 2852(s), 2113 (w), 2104(s), 1608(m), 1452(m), 1313(w), 1148(m), 1021(m), 739(s), 544(m).

4. Conclusion

The dinuclear cyano-bridged heterometallic Mn(III)–Fe(III) complex, $[Mn(salophen)(H_2O)_2][Mn(salophen)(H_2O)(\mu\text{-}NC)Fe(bbp)(CN)_2]\cdot 4H_2O$ (1), has been assembled by reaction of a Mn(III) precursor and the *mer*-tricyanometallate, $[Fe(bbp)(CN)_3]^{2-}$. The complex was characterized by chemical, spectroscopic, and structural analyses. Respective oxidation states of the metal centers as well as the chemical stability of the compound in DMSO solution was confirmed by UV/Vis spectroscopy, cyclic voltammetry, and CW X-band ESR spectroscopy. Low temperature magnetic studies revealed that dominant antiferromagnetic coupling is operative between the constituent cyano-bridged metal centers of 1, while ac magnetic susceptibility measurements manifest field induced single molecule magnetic behavior in 1. Further, UV-visible, electrochemical and ESR investigations demonstrated the interplay of a MMET process in 1 upon protonation. Thus, complex 1 is a unique example of cyano-bridged Mn^{III}–Fe^{III} dinuclear PBA exhibiting MMET and field induced SMM behavior. Thus, the present study paves the way for modulation of MMET characteristics in molecular PBAs by employing protonation as an external stimulant.

Author contributions

Prashurya Pritam Mudoi: conceptualization, carried out the experiments, data analysis (except magnetic data and EPR data), manuscript writing, review and editing, funding acquisition. Niku Ahmed, and Anup Choudhury: cyclic voltammetry measurement and data curation, review and editing of manuscript. Yanling Li and Rodrigue Lescouëzec: magnetic measurement, data curation, manuscript writing, editing and revision. Benjamin Kintzel, Oluseun Akintola and Winfried Plass: EPR measurement, data curation, manuscript writing, editing and revision. Rajendiran Marimuthu: Single crystal X-ray diffraction measurement and review and editing. Nayanmoni Gogoi: project design, conceptualization, methodology, validation, data curation, manuscript writing and revision, supervision, project administration, and funding acquisition.

Conflicts of interest

There are no conflicts to declare.

Data availability

All experimental data and results are available in the manuscript or SI: FT-IR, UV-visible & EPR spectra, powder X-ray diffraction, TGA patterns ESI-mass spectra, cyclic voltammograms. See DOI: https://doi.org/10.1039/d5dt01885d.

CCDC 2423285 (1) contains the supplementary crystallographic data for this paper.[50]

Acknowledgements

Authors gratefully acknowledged the generous financial support from ANRF, India (Sanction No. CRG/2021/005977).

Author also acknowledge Department of Science and Technology (DST), India and German Academic Exchange Service, DAAD for Indo-German Joint Research Project [Sanction No. DST/INT/DAAD/P-06/2022(G)]. PPM thanks Department of Science and Technology (DST), India for financial assistance under the DST-FIST (SR/FST/CS-I/2020/152) and PURSE programme [No. SR/PURSE/2022/143 (C)] to the Department of Chemistry, Dibrugarh University. The purchase of ESR equipment was enabled by the Deutsche Forschungsgemeinschaft (DFG, German Research Foundation, project number INST 275/406-1 FUGG) and the state of Thuringia.

References

1 L. Bogani and W. Wernsdorfer, *Nat. Mater.*, 2008, 7, 179–186.
2 R. Sessoli, H. L. Tsai, A. R. Schake, S. Wang, J. B. Vincent, K. Folting, D. Gatteschi, G. Christou and D. N. Hendrickson, *J. Am. Chem. Soc.*, 1993, 115, 1804–1816.
3 J. Bartolomé, F. Luis and J. F. Fernández, *Molecular Magnets: Physics and Applications*, Springer Berlin, Heidelberg, 2014.
4 A. K. Bar, P. Kalita, M. K. Singh, G. Rajaraman and V. Chandrasekhar, *Coord. Chem. Rev.*, 2018, 367, 163–216.
5 D. N. Woodruff, R. E. P. Winpenny and R. A. Layfield, *Chem. Rev.*, 2013, 113, 5110–5148.
6 O. Sato, T. Iyoda, A. Fujishima and K. Hashimoto, *Science*, 1996, 272, 704–705.
7 M. Nihei, *Chem. Lett.*, 2020, 49, 1206–1215.
8 T. Shiga, N. Mihara and M. Nihei, *Coord. Chem. Rev.*, 2022, 472, 214763.
9 J. Yadav, R. Kharel and S. Konar, *Coord. Chem. Rev.*, 2025, 523, 216283.
10 D. Li, R. Clérac, O. Roubeau, E. Harté, C. Mathoniere, R. Lé Bris and S. M. Holmes, *J. Am. Chem. Soc.*, 2008, 130, 252–258.
11 M. Nihei, Y. Sekine, N. Suganami, K. Nakazawa, A. Nakao, H. Nakao, Y. Murakami and H. Oshio, *J. Am. Chem. Soc.*, 2011, 133, 3592–3600.
12 (*a*) P. P. Mudoi, A. Choudhury, Y. Li, R. Lescouëzec, R. Marimuthu and N. Gogoi, *Inorg. Chem.*, 2021, 60, 17705–17714; (*b*) P. P. Mudoi, B. Sarma, A. Choudhury and N. Gogoi, *Dalton Trans.*, 2021, 50, 2057–2066.
13 Y. Li, A. Benchohra, B. Xu, B. Baptiste, K. Béneut, P. Parisiades, L. Delbes, A. Soyer, K. Boukheddaden and R. Lescouëzec, *Angew. Chem., Int. Ed.*, 2020, 59, 17272–17276.
14 R. J. Wei, R. Nakahara, J. M. Cameron, G. N. Newton, T. Shiga, H. Sagayama, R. Kumai, Y. Murakami and H. Oshio, *Dalton Trans.*, 2016, 45, 17104–17107.
15 B. Xu, Y. Li, G. Gontard, K. Béneut, P. Parisiades, M. Deutsch and R. Lescouëzec, *Inorg. Chem. Front.*, 2025, 12, 744–756.
16 M. Nihei, Y. Okamoto, Y. Sekine, N. Hoshino, T. Shiga, I. C. Liu and H. Oshio, *Angew. Chem., Int. Ed.*, 2012, 51, 6361–6364.
17 J. Li, S. Wu, S. Su, S. Kanegawa and O. Sato, *Chem. – Eur. J.*, 2020, 26, 3259–3263.
18 A. Zabala-Lekuona, J. M. Seco and E. Colacio, *Coord. Chem. Rev.*, 2021, 441, 213984.
19 T. T. Wang, M. Ren, S. S. Bao and L. M. Zheng, *Eur. J. Inorg. Chem.*, 2014, 1042–1050.
20 (*a*) H. Miyasaka, R. Clérac, W. Wernsdorfer, L. Lecren, C. Bonhomme, K. I. Sugiura and M. Yamashita, *Angew. Chem., Int. Ed.*, 2004, 43, 2801–2805; (*b*) C. J. Milios, A. Vinslava, W. Wernsdorfer, S. A. Moggach, S. Parsons, S. P. Perlepes, G. Christou and E. K. Brechin, *J. Am. Chem. Soc.*, 2007, 129, 2754–2755.
21 (*a*) R. Clérac, H. Miyasaka, M. Yamashita and C. Coulon, *J. Am. Chem. Soc.*, 2002, 124(43), 12837–12844; (*b*) H. Miyasaka, T. Madanbashi, A. Saitoh, N. Motokawa, R. Ishikawa, M. Yamashita, S. Bahr, W. Wernsdorfer and R. Clérac, *Chem. – Eur. J.*, 2012, 18, 3942–3954.
22 J. Kim, S. Han, I. K. Cho, K. Y. Choi, M. Heu, S. Yoon and B. J. Suh, *Polyhedron*, 2004, 23, 1333–1339.
23 T. Senapati, C. Pichon, R. Ababei, C. Mathonière and R. Clérac, *Inorg. Chem.*, 2012, 51, 3796–3812.
24 J. Glatz, J. R. Jiménez, L. Godefroy, H. J. von Bardeleben, L. Fillaud, E. Maisonhaute, Y. Li, L. M. Chamoreau and R. Lescouëzec, *J. Am. Chem. Soc.*, 2022, 144, 10888–10901.
25 I.-R. Jeon, S. Calancea, A. Panja, D. M. P. Cruz, E. S. Koumousi, P. Dechambenoit, C. Coulon, A. Wattiaux, P. Rosa, C. Mathonière and R. Clérac, *Chem. Sci.*, 2013, 4, 2463–2470.
26 S. Jia, X. Zhu and D. Li, *Dalton Trans.*, 2023, 52, 15009–15016.
27 A. Panja, P. Guionneau, I.-R. Jeon, S. M. Holmes, R. Clérac and C. Mathonière, *Inorg. Chem.*, 2012, 51, 12350–12359.
28 B. J. Kennedy and K. S. Murray, *Inorg. Chem.*, 1985, 24, 1552–1557.
29 P. Bhowmik, H. P. Nayek, M. Corbella, N. Aliaga-Alcalde and S. Chattopadhyay, *Dalton Trans.*, 2011, 40, 7916–7926.
30 P. Pérez-Lourido, J. Romero, L. Rodríguez, J. A. García-Vázquez, J. Castro, A. Sousa, J. R. Dilworth and O. R. Nascimento, *Inorg. Chem. Commun.*, 2002, 5, 337–339.
31 A. Panja, N. Shaikh, S. Gupta, R. J. Butcher and P. Banerjee, *Eur. J. Inorg. Chem.*, 2003, 1540–1547.
32 (*a*) F. P. Andrew and P. A. Ajibade, *Int. J. Electrochem. Sci.*, 2021, 16, 150950; (*b*) S. Biswas, K. Mitra, C. H. Schwalbe, C. R Lucas, S. K. Chattopadhyay and B. Adhikary, *Inorg. Chim. Acta*, 2005, 358, 2473–2481.
33 (*a*) K. A. Campbell, M. R. Lashley, J. K. Wyatt, M. H. Nantz and R. D. Britt, *J. Am. Chem. Soc.*, 2001, 123, 5710–5719; (*b*) K. P. Bryliakov, D. E. Babushkin and E. P. Talsi, *Mendeleev Commun.*, 1999, 9, 29–31.
34 H. Y. Kwak, D. W. Ryu, J. W. Lee, J. H. Yoon, H. C. Kim, E. K. Koh, J. Krinsky and C. S. Hong, *Inorg. Chem.*, 2010, 49, 4632–4642.
35 H. Zhou, Y. Wang, F. Mou, X. Shen and Y. Liu, *New J. Chem.*, 2014, 38, 5925–5934.

36 A. R. Sohn, K. S. Lim, D. W. Kang, J. H. Song, E. K. Koh, D. Moon and C. S. Hong, *Dalton Trans.*, 2016, 45, 19416–19427.
37 H. Y. Kwak, D. W. Ryu, H. C. Kim, E. K. Koh, B. K. Cho and C. S. Hong, *Dalton Trans.*, 2009, 11, 1954–1961.
38 T. Senapati, C. Pichon, R. Ababei, C. Mathonière and R. Clérac, *Inorg. Chem.*, 2012, 51, 3796–3812.
39 X. Shen, H. Zhou, J. Yan, Y. Li and H. Zhou, *Inorg. Chem.*, 2014, 53, 116–127.
40 H. Zhou, Y. Wang, F. Mou, X. Shen and Y. Liu, *Polyhedron*, 2015, 85, 457–466.
41 N. F. Chilton, R. P. Anderson, L. D. Turner, A. Soncini and K. S. Murray, *J. Comput. Chem.*, 2013, 34, 1164–1175.
42 H. Miyasaka, A. Saitoh and S. Abe, *Coord. Chem. Rev.*, 2007, 251, 2622–2664.
43 M. Haryono, M. Kalisz, R. Sibille, R. Lescouëzec, C. Fave, G. Trippe-Allard, Y. Li, M. Seuleiman, H. Rousselière, A. M. Balkhy, J.-C. Lacroix and Y. Journaux, *Dalton Trans.*, 2010, 39, 4751–4756.
44 S. Nastase, C. Maxim, M. Andruh, J. Cano, C. Ruiz-Pérez, J. Faus, F. Lloret and M. Julve, *Dalton Trans.*, 2011, 40, 4898–4908.
45 R. Ababei, C. Pichon, O. Roubeau, Y. G. Li, N. Bréfuel, L. Buisson, P. Guionneau, C. Mathonière and R. Clérac, *J. Am. Chem. Soc.*, 2013, 135, 14840–14853.
46 (*a*) M. Nihei, Y. Sekine, N. Suganami, K. Nakazawa, A. Nakao, H. Nakao, Y. Murakami and H. Oshio, *J. Am. Chem. Soc.*, 2011, 133, 3592–3600; (*b*) M. Nihei, K. Shiroyanagi, M. Kato, R. Takayama, H. Murakami, Y. Kera, Y. Sekine and H. Oshio, *Inorg. Chem.*, 2019, 58, 11912–11919.
47 R. A. Marcus, *Chem. Phys. Lett.*, 1987, 133, 471–477.
48 C. Duboc, *Chem. Soc. Rev.*, 2016, 45, 5834–5847.
49 S. Stoll and A. Schweiger, *J. Magn. Reson.*, 2006, 178, 42–55.
50 P. P. Mudoi, N. Ahmed, A. Choudhury, Y. Li, R. Lescouëzec, B. Kintzel, O. Akintola, W. Plass, M. Rajendiran and N. Gogoi, CCDC 2423285: Experimental Crystal Structure Determination, 2025, DOI: 10.5517/ccdc.csd.cc2mbmh3.